metals

MDPI

Article

Investigation on Mechanical Properties and Oxidation Behavior of 1.2 and 1.7 GPa Grades Coating-Free Press-Hardened Steels

Zhisong Chai [1], Qi Lu [2], Sarah Tedesco [3], Mingfeng Shi [3], Jason Coryell [3], Luke Reini [4], Qingquan Lai [5], Jianfeng Wang [2,*], Lingyu Wang [1,*] and Wei Xu [1]

[1] The State Key Laboratory of Rolling and Automation, Northeastern University, Shenyang 110189, China
[2] China Science Laboratory, General Motors Global Research and Development, Shanghai 201206, China
[3] Materials Engineering & Additive Design & Manufacture, General Motors Global Product Development, Purchasing & Supply Chain, Warren, MI 48092, USA
[4] Global Body Structures & Integrated Systems, General Motors Global Product Development, Purchasing & Supply Chain, Warren, MI 48092, USA
[5] Key Laboratory for Light-weight Materials, Nanjing Tech University, Nanjing 211816, China
* Correspondence: jeff.wang@gm.com (J.W.); wanglingyu@ral.neu.edu.cn (L.W.)

Abstract: Al-Si-coated boron-alloyed steels are the most widely used press-hardened steels (PHSs), which offers good oxidation resistance during hot forming due to the presence of the near eutectic Al-Si coating. In this study, a recently developed novel un-coated oxidation resistant PHS, called coating-free PHS (CF-PHS), is introduced as an alternative to the commercial Al-Si coated PHSs. With tailored additions of Cr, Mn, and Si, the new steel demonstrates superior oxidation resistance with a sub-micron oxide layer after the conventional hot stamping process. Hence, it does not require shot blasting before the subsequent welding and E-coating process. Two CF-PHS grades have been developed with ultimate tensile strengths of approximately 1.2 and 1.7 GPa, respectively. Both grades have a total elongation of 8–9%, exceeding the corresponding Al-Si-coated PHS grades (1.0 GPa/6–7%, 1.5 GPa/6–7%). Furthermore, the bendability of CF-PHS was similar to the corresponding Al-Si PHS grades. On the other hand, performance evaluations relevant to automotive applications, such as weldability, the E-coat adhesion, and tailor-welded hot stamp door ring, were also conducted on the CF-PHS steel to satisfy the requirements of manufacturing.

Keywords: press-hardened steels; mechanical properties; retained austenite; oxidation resistance

Citation: Chai, Z.; Lu, Q.; Tedesco, S.; Shi, M.; Coryell, J.; Reini, L.; Lai, Q.; Wang, J.; Wang, L.; Xu, W. Investigation on Mechanical Properties and Oxidation Behavior of 1.2 and 1.7 GPa Grades Coating-Free Press-Hardened Steels. *Metals* **2023**, *13*, 489. https://doi.org/10.3390/met13030489

Academic Editor: Marcello Cabibbo

Received: 31 December 2022
Revised: 5 February 2023
Accepted: 22 February 2023
Published: 27 February 2023

1. Introduction

As ultra-high strength structural materials, press-hardened steels (PHSs) are widely used for automotive body structure components to increase occupant safety and to simultaneously reduce mass for improved fuel economy and reduced CO_2 emission [1,2]. Currently, commercial PHSs can be mainly divided into bare and Al-Si-coated PHSs according to the oxidation problem because their production involves a high-temperature procedure. When the bared PHSs are exposed to the air at high temperatures, severe oxidation and decarbonization will inevitably occur, which causes a series of problems in the subsequent processes, such as die wear, extra shot blasting, and difficulty in welding [1,3]. Al-Si coating can be used to prevent the oxidation of bare PHSs at elevated temperatures, but its production cost is too high due to patent protection, welding difficulties, and reducing the service life of rollers in the furnace [4,5]. Therefore, a new cost-effective way to improve the oxidation resistance has been explored. In addition, although the final fully martensite microstructure endows a characteristic ultra-high strength for PHSs, it leads to poor ductility/toughness. Unfortunately, this combination of mechanical properties cannot successfully further promote the automobile's lightweight plan. Based on the above, a PHS with the combination of good high-temperature oxidation resistance and excellent mechanical properties has been actively developed.

The Cr alloying strategy is adopted by some researchers and applied in PHSs with excellent mechanical properties because Cr is an effective element to improve oxidation resistance. The first one is directly applying the high Cr stainless steel for the hot stamping process [6,7]. This not only obtains good oxidation resistance and does not need any coating, but also has excellent mechanical properties due to the transformation-induced plasticity (TRIP) effect. The other approach is to add only considerable quantities of Cr to medium-Mn steel with low austenitization temperature for hot stamping [8]. Utilizing the low heating temperature, combined with the Cr addition, can effectively reduce the oxidation rate. Moreover, based on the medium-Mn, steel has a lower martensite start (M_s) temperature, and C partitioning stabilizes untransformed austenite during the baking process [9,10]. The new Cr-alloyed medium-Mn steel has better tensile properties and great oxidation resistance after press hardening compared with the bare 22MnB5 PHS. Unfortunately, these PHSs are relatively expensive and have poor welding performance owing to the high alloying of Cr (~12–20 wt.%) or Mn (~5–10 wt.%), these PHSs have limited progress in industrial practice and commercial applications.

Based on the above research, the alloy content needs to be strictly controlled to improve welding performance and reduce the production cost of PHS. It has been demonstrated that adding an appropriate amount of Cr and Si can effectively improve high-temperature oxidation performance. There are two main reasons, the first one is that Si has stronger O affinity and higher thermal stability at elevated temperatures, which can form dense SiO_2 or SiO_2 and Fe_2SiO_4 [11,12]. The second one is that Si reduces the critical Cr content for the formation of a protective C_2O_3 [13–15]. These stable passive layers as diffusion barriers can be used to effectively inhibit the outward transport of metal ions and the inward transport of O. Moreover, some researchers [16,17] reported that Mn addition has a positive effect on high-temperature oxidation resistance compared to Mn-free alloys.

Beside oxidation resistance, tailoring Cr and Si addition can also enable the formation of beneficial retained austenite (RA), which can improve mechanical performance significantly via its TRIP effect [18,19]. During hot forming, auto-tempering of martensite takes place during quenching from M_s temperature to room temperature which remarkably reduces the cooling rate, so carbon can diffuse from martensite into adjacent austenite and stabilize it. This process is called dynamic carbon partitioning [20–22]. In traditional PHS, C partitions to austenite are not enough as most of the C will precipitate as cementite. Si addition can suppress cementite precipitation and promote the C dynamic partition during hot stamping [23]. As an austenite-stabilizing element, the addition of Cr can further increase the amount of RA during quenching [21]. Meanwhile, Cr can also reduce the diffusivity of carbon in austenite, which may slow austenite decomposition kinetics [24]. Furthermore, the synergetic effect of the Si and Cr in promoting greater RA retention is also reported [25].

Therefore, the synergistic addition of Cr, Si, and Mn should be considered when designing the composition of PHS. However, this idea has not been widely reported. In this study, two oxidation resistant coating-free PHSs (CF-PHSs) with tailored addition of Cr, Si and Mn have been developed with ultimate tensile strengths of approximately 1.2 and 1.7 GPa, respectively. Unlike Al-Si-coated PHS, direct laser welding of the 1.2 and 1.7 GPa CF-PHSs is able to produce tailor-welded blanks with excellent mechanical properties after hot forming. The oxidation resistance, microstructure, tensile properties, laser weldability, component three-point bending performances, and the high-temperature oxidation at component level of CF-PHS are evaluated and compared to existing bare or Al-Si-coated PHSs.

2. Experimental Procedures

2.1. Materials

The compositions of CF-PHS of 1.2 and 1.7 GPa grades are listed in Table 1, in which the commercial Al-Si-coated PHS grades of 1.0 GPa (Ductibor 1000) and 1.5 GPa (WA 1500) are also listed as comparison. The main difference in compositions of CF-PHS grades is

the C level. B and Ti are not added in the two CF-PHS grades since the hardenability is remarkably enhanced by the addition of Cr. To enable a global footprint, we collaborated with two steel makers in China and two steel makers in the US. All four steel makers successfully completed industry trials (>100 ton for each trial) of CF-PHS with 1.7 GPa tensile strength by either integrated or mini mill process. Regarding the CF-PHS with 1.2 GPa tensile strength, it was produced at a laboratory scale. The ingot was fabricated by a vacuum induction melting furnace and it was forged and cut into slabs with sectional dimensions of 150 × 120 mm. Subsequently, the slab was heated to 1200 °C for 6 h, and hot-rolled to 1.9 mm thickness with 7 passes. Finally, the plates were air-cooled to 650 °C and furnace cooling to room temperature for coiling simulation.

Table 1. Compositions of the designed and reference steels (wt.%).

Steel Grade	C	Mn	Cr	Si	Nb	B	Ti	Fe
1.2 GPa CF-PHS	0.08	1.5–2.5	≤2.5	≤1.5	0.025	-	-	Bal.
1.7 GPa CF-PHS	0.20	0.8–1.4	≤2.5	≤2.5	0.025	-	-	Bal.
1.0 GPa Al-Si coated PHS	0.10	1.80	-	0.30	0.04	0.003	0.02	Bal.
1.5 GPa Al-Si coated PHS	0.23	1.2	0.16	0.22	-	0.005	0.04	Bal.

2.2. Hot Forming Process

To reasonably design the austenitization temperature for the hot stamping process, the critical phase transformation temperatures, such as the austenite end transformation temperature (A_{c3}), martensite start temperature (M_s), and martensite finish temperature (M_f), were measured using a DIL805 A/D dilatometer. Specimens with dimensions of 1.4 mm × 10 mm × 4 mm were heated at 10 °C/s to 950 °C and held for 360 s, then cooled to room temperature at a cooling rate of 50 °C/s. The phase transformation temperatures of CF-PHSs are shown in Figure 1. The A_{c3}, M_s, and M_f temperatures of 1.2 GPa CF-PHS were 893, 445, and 260 °C, respectively. The A_{c3}, M_s, and M_f temperatures of 1.7 GPa CF-PHS were 879, 393, and 218 °C, respectively.

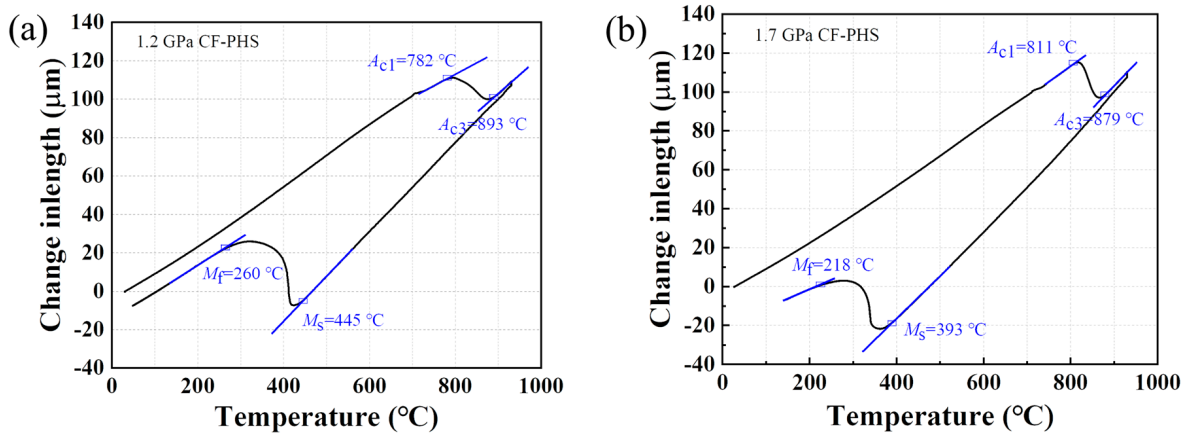

Figure 1. Dilatometric curves of CF-PHSs with (**a**) 1.2 GPa and (**b**) 1.7 GPa.

The schematic of industrial hot stamping and subsequent baking process are shown in Figure 2. The CF-PHS blanks with a thickness of approximately 1.9 mm were sheared from either the industry coils (1.7 GPa) or blanks from a laboratory heat (1.2 GPa). Then, they were subjected to austenitization at 930 °C for 6 min in a furnace with N_2, followed by die quenching with 4 MPa contact pressure, and finally baked at 170 °C for 20 min to simulate paint baking process.

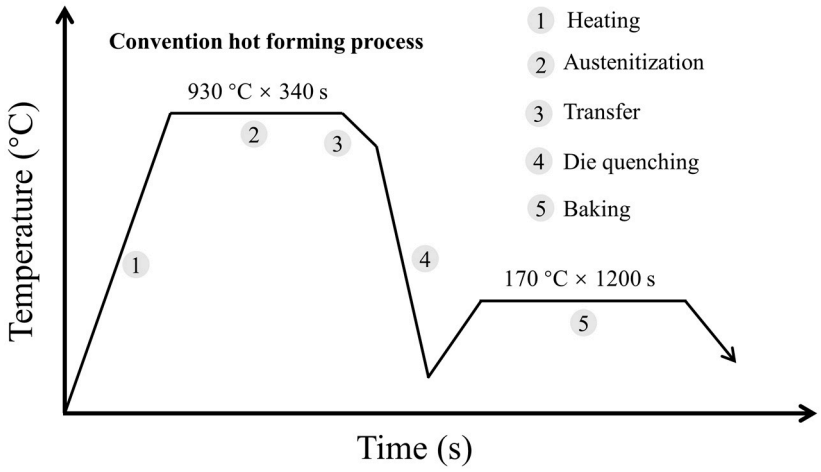

Figure 2. Schematic diagram of the hot forming process.

2.3. Microstructural Analyses and Mechanical Test

Oxide layers and microstructures were characterized by a field emission scanning electron microscope (FEG-SEM, Zeiss, Auriga Compact) with energy dispersive X-ray spectroscopy (EDS). SEM samples of microstructural observation were prepared by mechanical polish and etching with a solution of 4% nitric acid in ethanol. For preparing the oxide scale samples, the sample surfaces were protected by Al foil. The RA and prior austenite grain size (PAGS) were examined using electron backscatter diffraction (EBSD, Oxford) at 20 kV with a step size of 0.023 μm. The EBSD samples were prepared by electro-polished using a solution of 8.5% perchloric acid in ethanol. The PAGS was reconstructed by grain boundaries (between 15° and 60°) [26,27]. The equivalent PAGS was measured by the standard linear intercept method. The volume fraction of RA was measured from the diffraction intensity obtained by the X-ray diffraction (XRD, Bruker) with Co-Kα radiation. The amount of RA was calculated using the follow equation [28]:

$$V_\gamma = \frac{1.4I_\gamma}{I_\alpha + 1.4I_\gamma} \quad (1)$$

where V_γ is the volume fraction of RA, I_γ and I_α are the average integral intensity of the austenite and martensite peaks, respectively. The average integral intensity of the $(200)_\gamma$, $(220)_\gamma$, and $(311)_\gamma$ peaks was used to calculate the RA fraction.

The mechanical properties were assessed by uniaxial tensile tests f based on the ASTM E8 standard and by the instrumented three-point bending per VDA 238-100 [29]. All samples were prepared by electrical discharge machining (EDM). To eliminate the effect of oxide scale and decarburization layer, tensile and bending samples of CF-PHSs are grounded from 1.9 mm to 1.4 mm in thickness. Meanwhile, 1.4 mm thick samples of Al-Si-coated PHSs were used for performance comparison. All the tensile samples had the same dimension of 1.4 mm in thickness, 50 mm in gauge length, and 12.5 mm in width, with the longitudinal direction parallel to the sheet rolling direction. Tensile tests were carried out on an Instron 5984 test frame at an initial strain rate of 0.001/s. The bending angle is calculated by the punch displacement, when the maximum punch load is reached and unloaded. The experimental tool is mainly composed of two support rollers and indenters, of which the diameter of the support roller is 30 mm and the radius of the punch is 0.4 mm. Bending was conducted at a punch speed of 20 mm/min, with sample's rolling direction perpendicular to the bending axis to ensure the principal bending stress was along the sheet rolling direction. Component level quasi-static three-point bending tests were conducted on hot stamped prototype 1.9 mm thick door impact beams produced in a production line for 1.7 GPa coating-free PHS (1.86 mm) and 1.5 GPa Al-Si (1.90 mm)-coated PHS. Figure 3 shows the schematic diagram of part bending test. A semi-cylindrical punch with a radius of 152.4 mm was used to apply load on the top face of the door impact beam at a rate of

15 mm/min via displacement control. The distance between the two supports was 550 mm. Both punch force and displacement were digitally recorded at a sampling rate of 100 Hz.

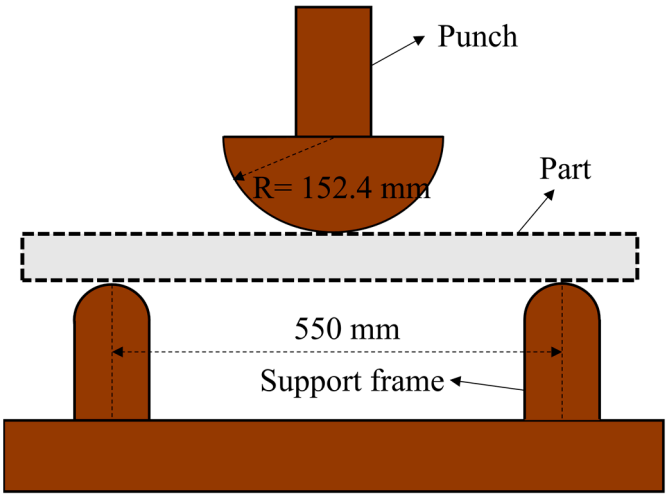

Figure 3. Schematic diagram of component level quasi-static three-point bending tests.

3. Results and Discussion

3.1. Oxide Scale

Figure 4 shows the cross-section morphology of oxide layers and corresponding to distribution of elements for coating-free and conventional PHSs under SEM combined with EDS. The high-temperature oxidation resistance of CF-PHSs and conventional PHSs exhibit significant differences. The oxide thickness of 1.2 and 1.7 GPa CF-PHSs was only several hundred of nanometers on the surface, while the commercial bare PHSs have approximately ten microns in thickness for oxide scale. In addition, the oxide layers of CF-PHSs were denser than those of commercial bare PHSs. EDS mapping shows that the oxides of CF-PHSs were enriched with Cr and Mn. Surprisingly, the Si-rich oxide was not detected, which may be relatively small. However, the enrichment of Si in oxide scale was found by EDS point, as shown in Figure 4c. In contrast, the oxide layers showed no enrichment of Cr, Si, and Mn in commercial bare PHS. These results prove that Cr, Si, and Mn can diffuse to the surface and combine with oxygen to form a very dense and thin oxide, which prevents the further oxidation of the steel substrate.

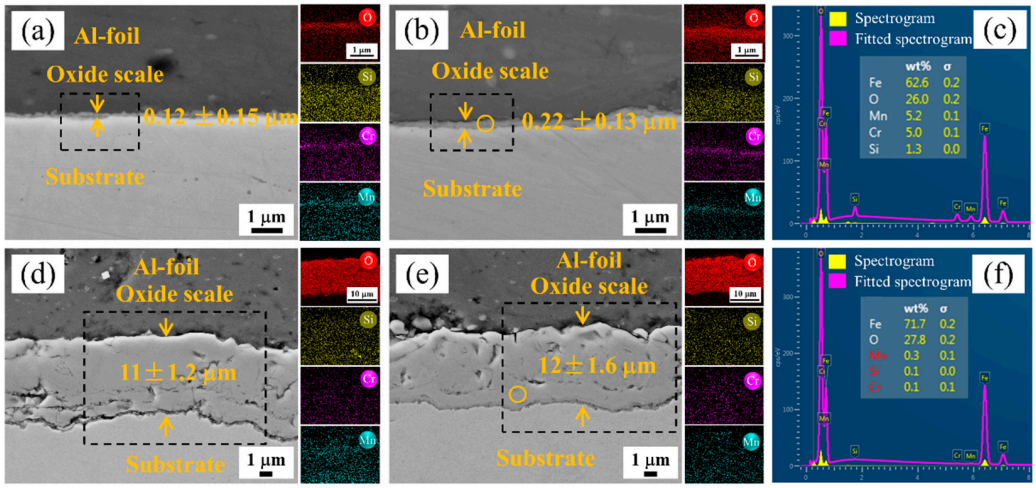

Figure 4. Cross-section morphology and EDS of the oxide of investigated and reference PHSs. (**a**) 1.2 GPa CF-PHS, (**b**) 1.7 GPa CF-PHS, (**c**) EDS point of oxide layers for 1.7 GPa CF-PHS, (**d**) 1.0 GPa bare PHS, (**e**) 1.5 GPa bare PHS, (**f**) EDS point of oxide layers for 1.5 GPa Al-Si bare PHS.

To get further insight into the composition of the oxide scales, identification of each oxide type in the scale is required. Here, the 1.7 GPa CF-PHS and 1.5 GPa bare PHS are taken as the representative for research. Figure 5 shows the diffraction spectrum of surface oxides formed on 1.7 GPa CF-PHS and 1.5 Gpa bare PHS. The Fe_2O_3 (JCPDS card no. 16-0653 and 21-0920) and Fe_3O_4 (JCPDS card no.89-0688 and 77-1545) phases were observed on both 1.5 GPa bare PHS and 1.7 GPa CF-PHS. However, oxides containing Cr, Mn, and Si in 1.7 GPa CF-PHS were not detected. which may be caused by the low amount or the signal being weaker compared to the other oxides. Therefore, further work will use more refined characterization for detection.

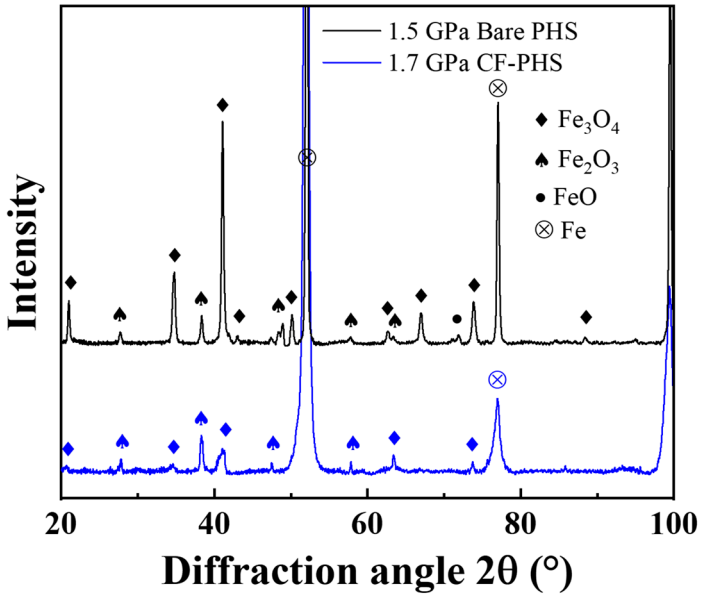

Figure 5. Diffraction pattern of 1.7 GPa coating-free steel and 1.5 GPa bare steel after oxidizing at 930 °C for 340 s.

3.2. Microstructure

Figure 6 shows the microstructural characteristics of CF-PHSs and reference PHSs. The microstructure of all PHSs is fully martensite, while the 1.7 GPa CF-PHS has some dispersed Cr-enriched carbide since the addition of Cr and medium C content. In the 1.2 GPa CF-PHS, the carbides are difficult to detect. This is probably due to: (a) the low carbon level limiting the amount of carbides formation; (b) the laboratory scale production not being able to effectively simulate the slow cooling process after the coiling of hot rolled coils, which allows sufficient time for carbide precipitation. The prior austenite grain structures of all PHSs are shown in Figure 6a,d,j,g. The average prior austenite grain size (PAGS) of the 1.2 GPa and 1.7 GPa CF-PHS were approximately 15.2 and 5.7 μm, respectively. The large PAGS of the 1.2 GPa grade is mainly attributed to the insufficient amount of Cr carbides and Nb carbides which provide grain boundary pinning during austenitization [30–33]. It has a similar PAGS with the 1.0 GPa Al-Si-coated PHS without carbide (~13 μm) under the same hot stamping condition. The carbides in 1.7 GPa CF-PHS have a significant effect on grain refinement. RA was found in both CF-PHS compared with conventional PHSs, as indicated by Figure 3c,f, due to the tailored addition of Cr and Si. Si addition can prohibit the formation of cementite during die quench. The addition of Cr increases the local carbon enrichment in the interface of austenite and martensite. Thus, the dynamic partitioning of carbon can be effectively improved and RA can be stabilized during die quenching process.

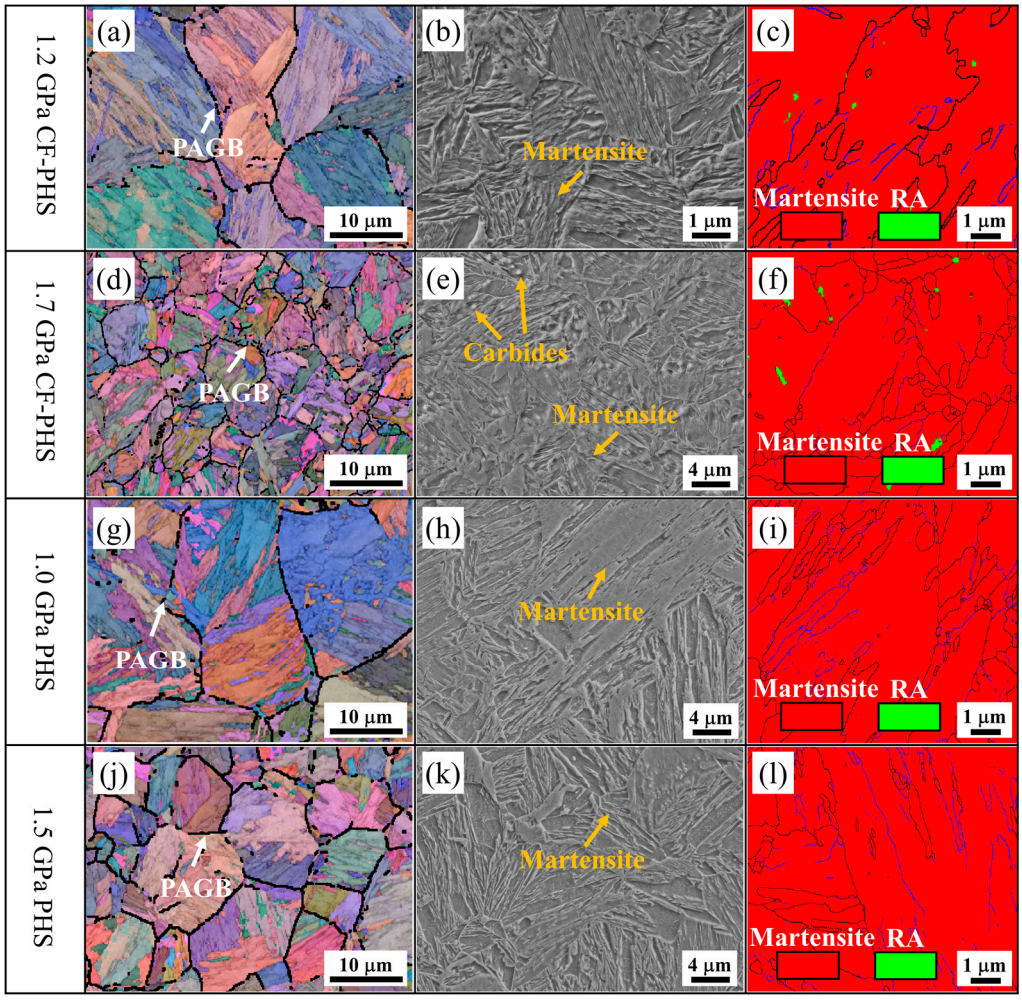

Figure 6. Grain size distribution and microstructure of the all PHSs. (**a**,**d**) PAGSs, (**b**,**e**) microstructure, (**c**,**f**) EBSD mappings of the 1.2 and 1.7 GPa CF-PHS, respectively. (**g**,**j**) PAGSs, (**h**,**k**) microstructure, (**i**,**l**) EBSD mappings of the 1.0 and 1.5 GPa Al-Si-coated PHS, respectively. RA and martensite were marked by green and red color, respectively.

To further confirm the volume fraction of RA in investigated and reference PHSs, XRD was used for measurement. Figure 7 shows the XRD diffraction pattern for all PHSs. The austenite content of both CF-PHSs is approximately 4–5 vol.% according to XRD results. However, there is no austenite peak detected in 1.0 and 1.5 GPa Al-Si-coated PHSs, which indicates that there is no RA in their microstructure.

3.3. Tensile Properties and Bending Performance

The tensile properties of CF-PHSs and Al-Si-coated PHSs are presented in Figure 8a, and the results of the tensile properties are summarized in Table 2. CF-PHSs have not only higher ultimate tensile strength (1.73 GPa vs. 1.55 GPa, 1.23 GPa vs. 1.08 GPa) but also better ductility (8.5% vs. 6.5%, 8.5% vs. 6.2%) than Al-Si-coated PHSs at their corresponding strength levels. The higher ultimate tensile strength could be mainly attributed to the solid solution strengthening effect of Si [23] and grain refinement [34], while the higher ductility is mainly contributed by the presence of RA through the TRIP effect during deformation, and the fine PAGS only has a slight improvement in ductility [21]. For automotive body-in-white applications, a tensile property is only one of the required mechanical properties. Bending performance is also a factor of great importance, since fracture of body structural components most likely first occurs under deformation modes that are close to bending during a crash event. The bending performance of the CF-PHSs and Al-Si-coated PHSs

was evaluated at coupon level per VDA 238-100, and the results are shown in Figure 8b. Even at a 30.0% higher peak force (11,844 N vs. 9112 N), the bending angle of the 1.7 GPa CF-PHS (60°) was still similar to that of the Al-Si-coated PHS (57°) with a 1.5 GPa tensile strength. Regarding the 1.2 GPa CF-PHS, its bending angle (79°) is lower than the (88°), but its peak force (9104 N vs. 7015 N) is 29.9% higher than that of the 1.0 GPa Al-Si-coated PHS. The 1.2 GPa CF-PHS coupons were taken from a laboratory scale hot rolled blanks, and it is expected that the bending performance will further be improved when this steel was made by production scale equipment.

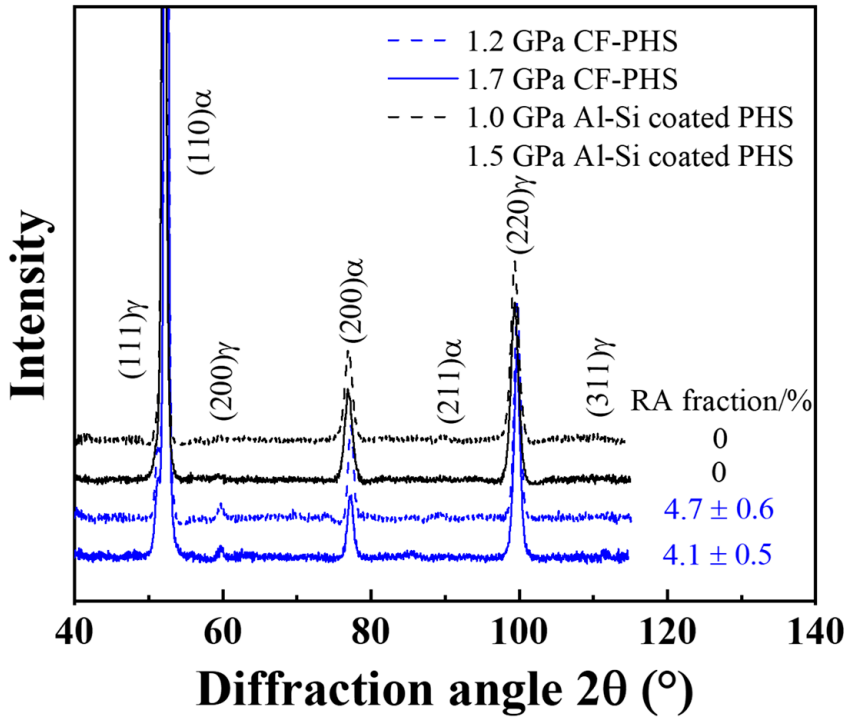

Figure 7. XRD pattern showing the peaks of austenite and martensite for all PHSs.

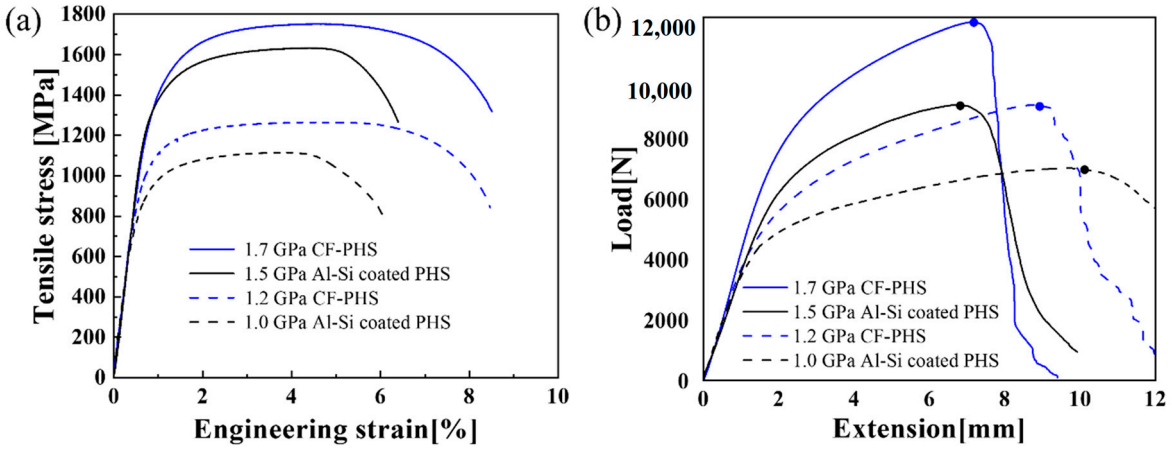

Figure 8. Tensile (**a**) and bending (**b**) performances of the investigated PHSs and reference PHSs.

Table 2. Mechanical properties of CF-PHSs and commercial Al-Si PHS.

Steel	UTS (MPa)	TEL (%)	Peak Force (N)	Bending Angle (°)
1.2 GPa CF-PHS	1236 ± 6	8.4 ± 0.5	9104 ± 53	79 ± 1.2
1.7 GPa CF-PHS	1731 ± 8	8.5 ± 0.4	11,844 ± 87	60 ± 0.6
1.0 GPa Al-Si-coated PHS	1086 ± 4	6.5 ± 0.3	7015 ± 68	88 ± 0.5
1.5 GPa Al-Si-coated PHS	1552 ± 6	6.2 ± 0.5	9112 ± 82	57 ± 0.9

3.4. Tailored Laser Welding and E-Coat Adhesion Performance

Without use of a filler wire or laser ablation, direct laser welding was also carried out for CF-PHS with the combination of 1.7 GPa/1.7 GPa and 1.7 GPa/1.2 GPa. The 1.7 GPa and 1.2 GPa CF-PHS blanks have the same thickness (~1.83 mm). Their tensile performances after hot forming are shown in Figure 9. After the tensile test, all the samples were fractured in the base materials, indicating a good weld seam performance.

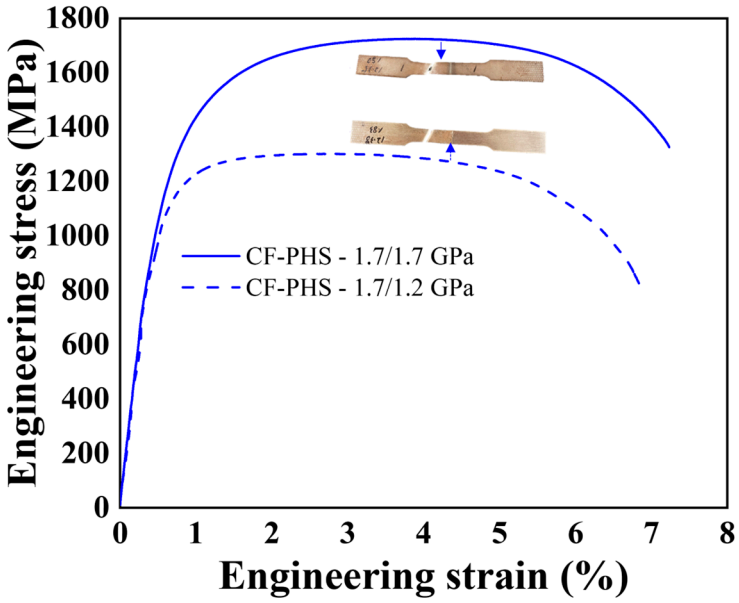

Figure 9. Tensile properties of tailor-welded CF-PHS with the combination of 1.7 GPa/1.7 GPa and 1.7 GPa/1.2 GPa after hot forming. All the samples broke in the base metal after tensile tests.

To evaluate the E-coat adhesion,1.5 GPa bare PHS after shot blasting, 1.5 GPa Al-Si coated PHS, and 1.7 GPa CF-PHS without shot blasting were first phosphated and then E-coated. Figure 10 shows the macroscopic morphology of these PHSs subjected to stone chip and tap adhesion testing. Coating adhesion was evaluated according to the stone chip testing standard (GMW14700) and tape adhesion testing standard (GMW14829). The results showed similar performance between all three materials in both the stone ship and tap adhesion tests, indicating a good adhesion of CF-PHS can be achieved with an ultrathin surface oxide.

3.5. Mechanical Properties and High-Temperature Oxidation of Components Level

Component level three-point bending tests were also conducted using a prototype hot stamped door impact beam of 1.83 mm thickness. The 1.90 mm 1.5 GPa Al-Si coated PHS was used for comparison. As shown in Figure 11, the 1.7 GPa CF-PHS (31.6 kN @ 25.8 mm) has both a higher peak force and a larger displacement at peak load than that of the regular Al-Si-coated PHS 1.5 GPa (29.3 kN @ 24.3 mm). The excellent component performance agrees well with coupon-level tensile and bending performances. CF-PHS even at a lower thickness has a much higher energy absorption capability (represented by the product of the peak load and displacement at peak load), about 10.9% higher than the

Al-Si-coated PHS. Therefore, a combination of high strength and good toughness in the CF-PHS leads to an excellent energy absorption capability at component level. Therefore, potential light-weighting opportunities exist by replacing the commercial Al-Si coated PHS with the CF-PHS by down-gaging components while maintaining the same energy absorption capability.

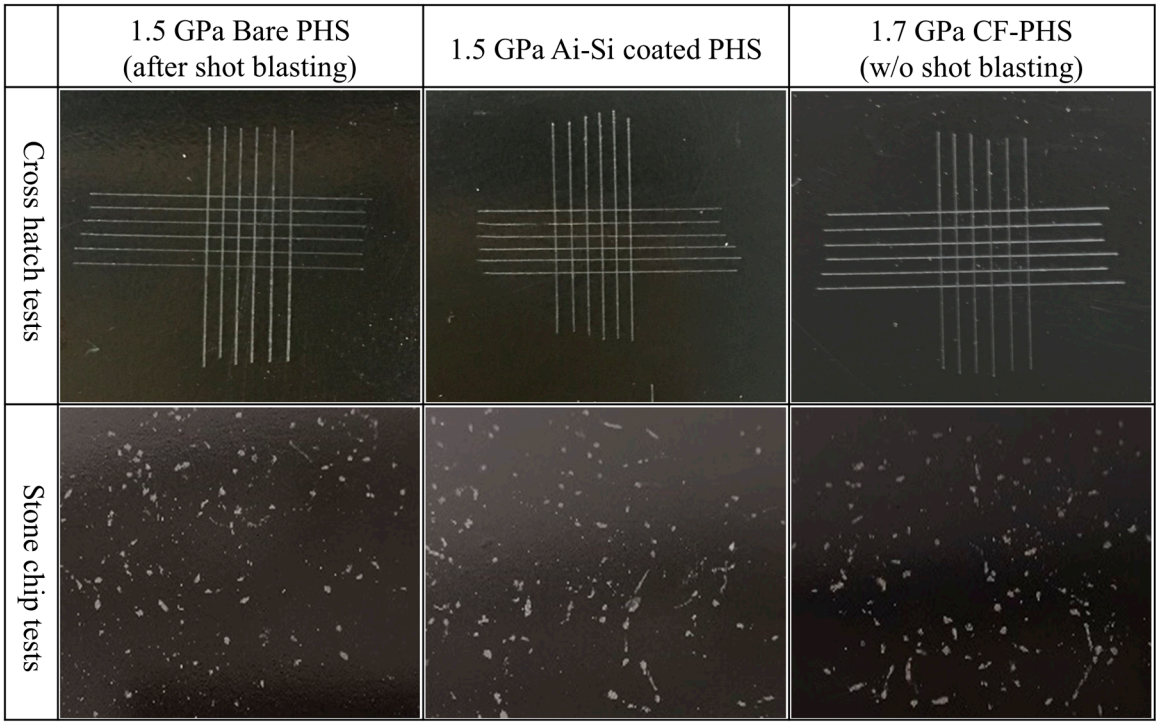

Figure 10. E-coat adhesion comparison of 1.5 GPa bare PHS, 1.5 GPa Al-Si coated PHS, and 1.7 GPa CF-PHS.

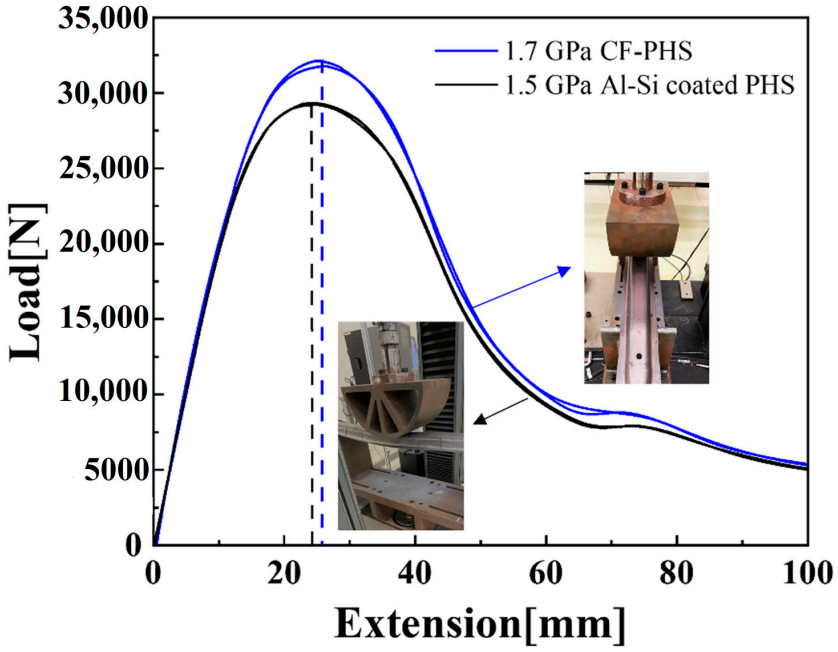

Figure 11. Component level three-point bending curves of prototype door impact beams for 1.7 GPa CF-PHS and 1.5 GPa Al-Si-coated PHS.

Tailor hot stamped laser-welded door ring is one of the most promising methods to save weight, while maintaining crashworthiness. Therefore, a reduced version (3:4 ratio) of an automobile integrated welding door ring was designed for hot stamping. The whole door ring materials were welded for coating-free with a combination of 1.7 GPa/1.7 GPa and 1.7 GPa/1.2 GPa, while the Al-Si coated PHS with a combination of 1.5 GPa/1.5 GPa for comparison. Figure 12 shows the macroscopic morphology, the thickness of scale oxide, and microstructure of laser-welded blank door ring after hot forming for CF-PHSs and 1.5 GPa bare PHS. It can be seen that the macro surfaces of 1.5 GPa bare PHS and CF-PHSs show significant differences. Compared with 1.5 GPa bare PHS (the thickness of oxide scale, ~13 μm), the surface quality of the integrated door ring formed by hot forming without coating was excellent, and the thickness of the oxide scale was only 200–300 nm. In addition, the ferrite and bainite microstructure were found in CF-PHSs, which indicates that they have low critical cooling rates.

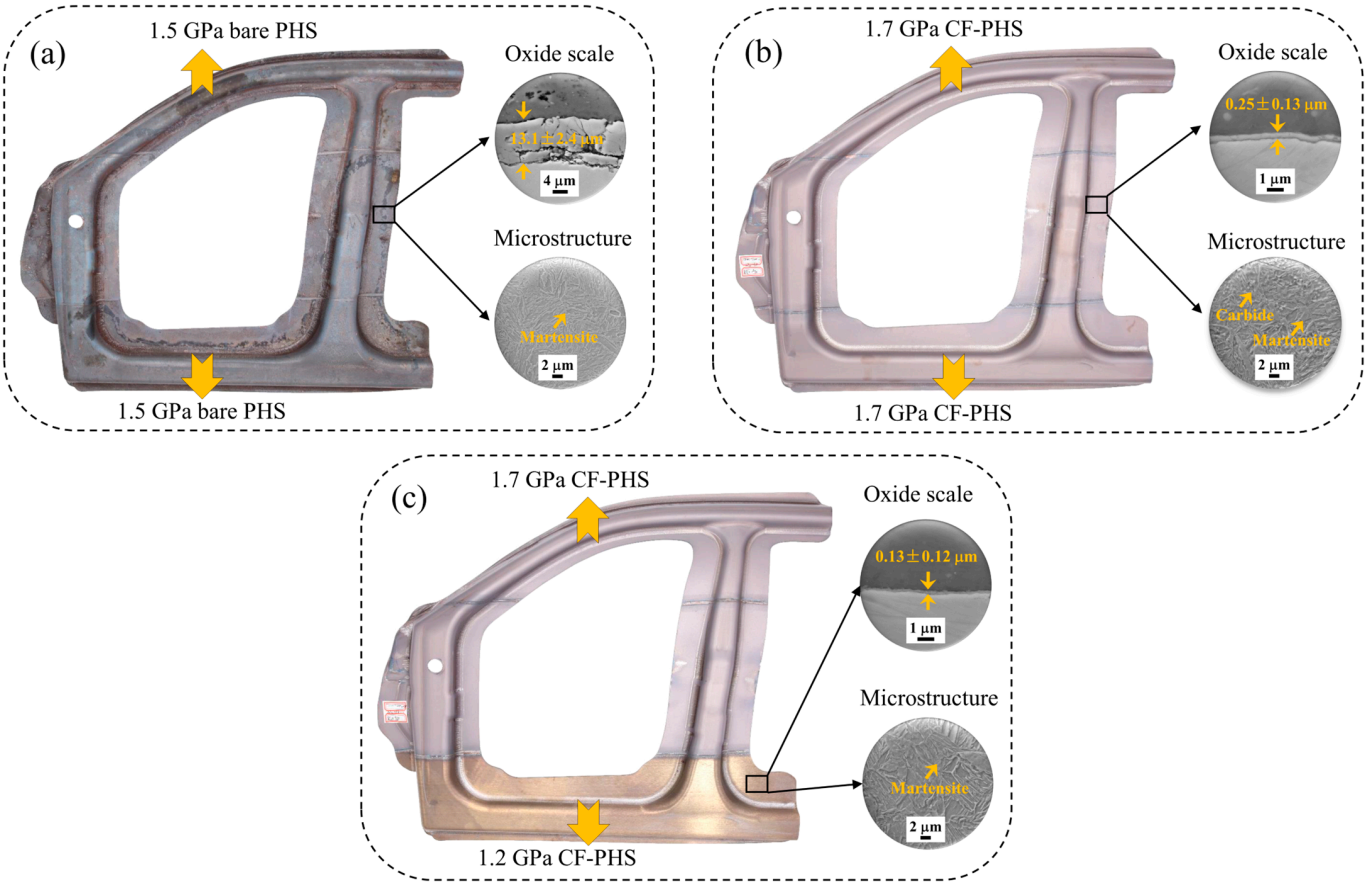

Figure 12. Tailor-welded blanks after hot forming of (**a**) bare PHS with 1.5 GPa/1.5 GPa and CF-PHSs with (**b**) 1.7 GPa/1.7 GPa and (**c**) 1.7 GPa/1.2 GPa.

4. Summary

In this work, the novel oxidation-resistant CF-PHSs with 1.2 and 1.7 GPa tensile strengths were developed. The tensile properties, bending performance, and high-temperature oxidation resistance subjected to hot stamping were investigated. In addition, the performance tests of component level were also conducted, such as laser weldability, E-coat adhesion properties, mechanical properties, and oxidation resistance. The conclusions are as follows:

1. The tailored Cr, Si, and Mn promote the formation of Cr- and Si-enriched dense surface oxide, leading to an excellent oxidation resistance at high temperatures.
2. A primarily martensitic with retained austenite is found in both 1.2 and 1.7 GPa CF-PHS grades after the conventional hot stamping process since the tailored Cr and

Si addition promotes the carbon partitioning from martensite to austenite during die quenching. The featured microstructure results in excellent tensile and bending performances at both coupon and component levels.

3. Initial laser welding results indicated that direct laser welding can be applied for tailored-welded blank application without using filler wire and/or laser ablation, both of which are currently adopted for the laser welding of Al-Si-coated PHS.
4. CF-PHS with an ultra-thin surface oxide has sufficient E-coat adhesion compared to the existing counterparts based on the cross hatch and stone chip testing.

Author Contributions: Conceptualization, J.W. and L.W.; methodology, Z.C.; software, Z.C.; validation, Q.L. (Qi Lu), S.T. and M.S.; formal analysis, Z.C. and Q.L. (Qi Lu).; investigation, Z.C. and Q.L. (Qingquan Lai); resources, L.W. and W.X.; data curation, J.W. and L.R.; writing—original draft preparation, Z.C.; writing—review and editing, J.W. and Q.L. (Qi Lu); visualization, J.C.; supervision, L.W.; project administration, W.X.; funding acquisition, W.X. All authors have read and agreed to the published version of the manuscript.

Funding: This work was financially supported by the National Natural Science Foundation of China (Grant Nos. U22A20106 and 52201112), and the China Postdoctoral Science Foundation (Grant No. 2022M710627).

Institutional Review Board Statement: Not applicable.

Informed Consent Statement: Not applicable.

Data Availability Statement: Not applicable.

Acknowledgments: The authors would like to thank Jinlong Zhu for preparing the mechanical test specimens for this study.

Conflicts of Interest: The authors declare no conflict of interest.

References

1. Karbasian, H.; Tekkaya, A. A review on hot stamping. *J. Mater. Process. Technol.* **2010**, *210*, 2103–2118. [CrossRef]
2. Billur, E. *Hot Stamping of Ultra High-Strength Steels*; Springer: Cham, Switzerland, 2019.
3. Mori, K.; Bariani, P.; Behrens, B.-A.; Brosius, A.; Bruschi, S.; Maeno, T.; Merklein, M.; Yanagimoto, J. Hot stamping of ultra-high strength steel parts. *CIRP Ann.* **2017**, *66*, 755–777. [CrossRef]
4. Ighodaro, O.; Biro, E.; Zhou, Y. Comparative effects of Al-Si and galvannealed coatings on the properties of resistance spot welded hot stamping steel joints. *J. Mater. Process. Technol.* **2016**, *236*, 64–72. [CrossRef]
5. Wang, Z.; Cao, Z.; Wang, J.; Huang, M. Improving the bending toughness of Al-Si coated press-hardened steel by tailoring coating thickness. *Scr. Mater.* **2021**, *192*, 19–25. [CrossRef]
6. Santacreu, P.-O.; Badinier, G.; Moreau, J.-B.; Herbelin, J.-M. Fatigue Properties of a New Martensitic Stainless Steel for Hot Stamped Chassis Parts. *SAE Tech. Pap.* **2015**. [CrossRef]
7. Wang, L.J.; Liu, C.M. Martensitic Stainless Steel as Alternative for Hot Stamping Steel with High Product of Strength and Ductility. *Adv. Mater. Res.* **2015**, *1063*, 37–41. [CrossRef]
8. Li, S.; Wen, P.; Li, S.; Song, W.; Wang, Y.; Luo, H. A novel medium-Mn steel with superior mechanical properties and marginal oxidization after press hardening. *Acta Mater.* **2021**, *205*, 116567. [CrossRef]
9. Hou, Z.; Opitz, T.; Xiong, X.; Zhao, X.; Yi, H. Bake-partitioning in a press-hardening steel. *Scr. Mater.* **2019**, *162*, 492–496. [CrossRef]
10. Lu, Q.; Eizadjou, M.; Wang, J.; Ceguerra, A.; Ringer, S.; Zhan, H.; Wang, L.; Lai, Q. Medium-Mn Martensitic Steel Ductilized by Baking. *Met. Mater. Trans. A* **2019**, *50*, 4067–4074. [CrossRef]
11. Cai, X.; Ding, S.; Jin, S.; Xu, L.; Liu, G.; Sun, B.; Shen, T. Superior high-temperature oxidation resistance of nanocrystalline 304 austenitic stainless steel containing a small amount of Si. *Scr. Mater.* **2021**, *204*, 114155. [CrossRef]
12. Zhang, L.; Yan, W.; Shi, Q.; Li, Y.; Shan, Y.; Yang, K. Silicon enhances high temperature oxidation resistance of SIMP steel at 700 °C. *Corros. Sci.* **2020**, *167*, 108519. [CrossRef]
13. Yun, D.W.; Seo, S.; Jeong, H.; Yoo, Y. The effects of the minor alloying elements Al, Si and Mn on the cyclic oxidation of Ni–Cr–W–Mo alloys. *Corros. Sci.* **2014**, *83*, 176–188. [CrossRef]
14. Tökei, Z.; Viefhaus, H.; Grabke, H. Initial stages of oxidation of a 9CrMoV-steel: Role of segregation and martensite laths. *Appl. Surf. Sci.* **2000**, *165*, 23–33. [CrossRef]
15. Wang, S.; Wu, Y.; Ni, C.; Niu, Y. The effect of Si additions on the high temperature oxidation of a ternary Ni–10Cr–4Al alloy in 1atm O_2 at 1100 °C. *Corros. Sci.* **2009**, *51*, 511–517. [CrossRef]

16. Chen, S.; Jin, X.; Rong, L. Improvement in High Temperature Oxidation Resistance of 9% Cr Ferritic–Martensitic Steel by Enhanced Diffusion of Mn. *Oxid. Met.* **2016**, *85*, 189–203. [CrossRef]
17. Jin, X.; Chen, S.; Rong, L. Effects of Mn on the mechanical properties and high temperature oxidation of 9Cr2WVTa steel. *J. Nucl. Mater.* **2017**, *494*, 103–113. [CrossRef]
18. Fischer, F.; Reisner, G.; Werner, E.; Tanaka, K.; Cailletaud, G.; Antretter, T. A new view on transformation induced plasticity (TRIP). *Int. J. Plast.* **2000**, *16*, 723–748. [CrossRef]
19. Zhang, C.; Xiong, Z.; Yang, D.; Cheng, X. Heterogeneous quenching and partitioning from manganese-partitioned pearlite: Retained austenite modification and formability improvement. *Acta Mater.* **2022**, *235*, 118060. [CrossRef]
20. Chai, Z.; Lu, Q.; Hu, J.; Wang, L.; Wang, Z.; Wang, J.; Xu, W. Effect of retained austenite on the fracture behavior of a novel press-hardened steel. *J. Mater. Sci. Technol.* **2023**, *135*, 34–45. [CrossRef]
21. Wei, X.; Chai, Z.; Lu, Q.; Hu, J.; Liu, Z.; Lai, Q.; Wang, J.; Xu, W. Cr-alloyed novel press-hardening steel with superior combination of strength and ductility. *Mater. Sci. Eng. A* **2021**, *819*, 141461. [CrossRef]
22. Chang, Z.; Li, Y.; Wu, D. Enhanced ductility and toughness in 2000 MPa grade press hardening steels by auto-tempering. *Mater. Sci. Eng. A* **2020**, *784*, 139342. [CrossRef]
23. Linke, B.M.; Gerber, T.; Hatscher, A.; Salvatori, I.; Aranguren, I.; Arribas, M. Impact of Si on Microstructure and Mechanical Properties of 22MnB5 Hot Stamping Steel Treated by Quenching & Partitioning (Q&P). *Met. Mater. Trans. A* **2018**, *49*, 54–65. [CrossRef]
24. Kirchner, G.; Nishizawa, T.; Uhrenius, B. The distribution of chromium between ferrite and austenite and the thermodynamics of the α/γ equilibrium in the Fe-Cr and Fe-Mn Systems. *Met. Mater. Trans. B* **1973**, *4*, 167–174. [CrossRef]
25. Pierce, D.; Coughlin, D.; Clarke, K.; De Moor, E.; Poplawsky, J.; Williamson, D.; Mazumder, B.; Speer, J.; Hood, A.; Clarke, A. Microstructural evolution during quenching and partitioning of 0.2C-1.5Mn-1.3Si steels with Cr or Ni additions. *Acta Mater.* **2018**, *151*, 454–469. [CrossRef]
26. Kinoshita, Y.; Yardley, V.; Tsurekawa, S. Relation between microstructures of martensite and prior austenite in 12 wt% Cr ferritic steel. *J. Mater. Sci.* **2011**, *46*, 4261–4269. [CrossRef]
27. Kitahara, H.; Ueji, R.; Tsuji, N.; Minamino, Y. Crystallographic features of lath martensite in low-carbon steel. *Acta Mater.* **2006**, *54*, 1279–1288. [CrossRef]
28. Atkins, E. Elements of X-ray Diffraction. *Phys. Bull.* **1978**, *29*, 572. [CrossRef]
29. Noder, J.; Abedini, A.; Butcher, C. Evaluation of the VDA 238–100 Tight Radius Bend Test for Plane Strain Fracture Characterization of Automotive Sheet Metals. *Exp. Mech.* **2020**, *60*, 787–800. [CrossRef]
30. Kong, L.; Liu, Y.; Liu, J.; Song, Y.; Li, S.; Zhang, R.; Li, T.; Liang, Y. The influence of chromium on the pearlite-austenite transformation kinetics of the Fe–Cr–C ternary steels. *J. Alloys Compd.* **2015**, *648*, 494–499. [CrossRef]
31. Jung, S.; Sohn, S.S.; Jo, Y.H.; Choi, W.-M.; Lee, B.-J.; Oh, Y.-J.; Kim, G.-Y.; Jang, S.; Lee, S. Effects of Cr and Nb addition on high-temperature tensile properties in austenitic cast steels used for turbo-charger application. *Mater. Sci. Eng. A* **2016**, *677*, 316–324. [CrossRef]
32. Yoo, J.; Jo, M.C.; Bian, J.; Sohn, S.S.; Lee, S. Effects of Nb or (Nb + Mo) alloying on Charpy impact, bending, and delayed fracture properties in 1.9-GPa-grade press hardening steels. *Mater. Charact.* **2021**, *176*, 111133. [CrossRef]
33. Chen, W.; Gao, P.; Wang, S.; Zhao, X.; Zhao, Z. Strengthening mechanisms of Nb and V microalloying high strength hot-stamped steel. *Mater. Sci. Eng. A* **2020**, *797*, 140115. [CrossRef]
34. Morito, S.; Yoshida, H.; Maki, T.; Huang, X. Effect of block size on the strength of lath martensite in low carbon steels. *Mater. Sci. Eng. A* **2006**, *438–440*, 237–240. [CrossRef]